

# Oxalic Acid-Assisted Vacancy Engineering Promotes Iron–Copper Sulfide Nanosheets for High-Current Density Water Oxidation

Fengli Wei, Jinghao Shen, Junlin Gong, Qimin Peng, Luyan Shi, Tayirjan Taylor Isimjan,\* and Xiulin Yang\*



Cite This: *J. Phys. Chem. Lett.* 2024, 15, 1172–1180



Read Online

ACCESS |



Metrics & More



Article Recommendations



Supporting Information

**ABSTRACT:** The effective defect and interface coupling are pivotal for the promotion of the catalytic activity for the oxygen evolution reaction. Herein, we report novel hybrid nanosheets with sulfur vacancies composed of  $\text{FeS}_2$  and  $\text{Cu}_{39}\text{S}_{28}$  grown on Cu foam ( $\text{V}_s\text{-FeS}_2/\text{Cu}_{39}\text{S}_{28}$ ). The optimal  $\text{V}_s\text{-FeS}_2/\text{Cu}_{39}\text{S}_{28}$  exhibits a high current output of  $500 \text{ mA cm}^{-2}$  at a low overpotential of 370 mV and robust stability for 60 h at  $100 \text{ mA cm}^{-2}$ , surpassing the values of most previously reported Cu-based catalysts. Furthermore, a two-electrode electrolyzer made by pairing the prepared catalyst with commercial Pt/C requires a low cell voltage of 1.75 V at  $100 \text{ mA cm}^{-2}$  and is retained over 80 h. Key to its excellent performance is the synergism between intertwined  $\text{FeS}_2$  and  $\text{Cu}_{39}\text{S}_{28}$  domains, enriched by the deliberate introduction of sulfur vacancies, thus optimizing the electronic structure and causing the proliferation of catalytic active sites. This work presents a potent Cu-based electrocatalyst and emphasizes the leveraging of non-precious metals for efficient water oxidation.



Electrochemical water splitting as an emission-free technology for producing high-purity hydrogen in a green manner is booming on the avenue to large-scale application.<sup>1,2</sup> However, the anodic oxygen evolution reaction (OER) is identified as the obstacle in water splitting, as it involves sluggish kinetics of the rigid O=O bond and multiple proton-coupled electron transfer steps with high energy barriers.<sup>3,4</sup> Currently, widespread application of state-of-the-art OER catalysts (i.e.,  $\text{RuO}_2$  and  $\text{IrO}_2$ ) has been severely restricted by their relatively scarce nature and accompanying exorbitant prices.<sup>5</sup> Accordingly, understanding the underlying limits and exploiting cost-effective nonprecious OER catalysts for upgrading modern energy devices toward commercialization are exigent.

Transition metal-based compounds are viable alternatives to conventional noble metal catalysts, owing to their abundance and appropriate electronic structure.<sup>6,7</sup> Among them, Cu-based materials have repeatedly been reported to be promising catalysts for the OER when considering their cost and notable redox properties.<sup>8</sup> For example, Ren et al. achieved an overpotential of only 317 mV at  $25 \text{ mA cm}^{-2}$  using Cu(tetracyanoquinodimethane) nanoarrays on Cu foam (CF).<sup>9</sup> As an imperative Cu-based material, copper sulfide species have a strong capacity to obtain electrons because of the abundant electron holes in the 3p orbital in S, which results in strong plasticity in electrochemical water splitting.<sup>10</sup> However, individual copper sulfide species struggle to achieve the high current densities at low overpotentials due to the larger charge transfer resistance ( $R_{ct}$ ), weak absorption capacity for oxygen-containing intermediates, low adsorption energy for

water,<sup>11,12</sup> etc., such as covellite CuS nanocrystals<sup>13</sup> and nanosheet-shaped CuS (NS-CuS).<sup>14</sup>

In recent years, a variety of synthetic methods and optimized strategies have been designed to enhance the activity of copper sulfide-based hybrid nanostructures. Coupling a highly conductive and stable component through interfacial interaction can modulate the electronic structure, generate more appropriate active sites, and accelerate the electron transfer rate, thereby ameliorating OER performance.<sup>15–17</sup> For instance, comparable efforts have been devoted to investigating copper sulfide-based composites, including  $\text{Cu}_7\text{S}_4/\text{MoS}_2$  nanoframes,<sup>18</sup>  $\text{CuS-Ni}_3\text{S}_2$  nanodisks,<sup>19</sup>  $\text{Cu}_{1.96}\text{S}/\text{Co}_9\text{S}_8$  nanoparticles,<sup>20</sup> etc. However, complex processes and costly materials hinder their practical use, which sparked our interest in uncovering the catalytic enhancement mechanisms. Iron, the second most abundant metallic element in the Earth's crust (5.6%), is both nontoxic and inexpensive.<sup>21,22</sup> The growing research interest in iron-containing catalysts stems from their adaptable physical and chemical properties. Guided by the concept of interfacial coupling, we designed bimetallic catalysts with high activity, capitalizing on the distinct attributes of Fe and Cu metals. Notably, vacancy engineering is generally considered to be feasible for increasing the density of active

**Received:** November 19, 2023

**Revised:** January 4, 2024

**Accepted:** January 19, 2024

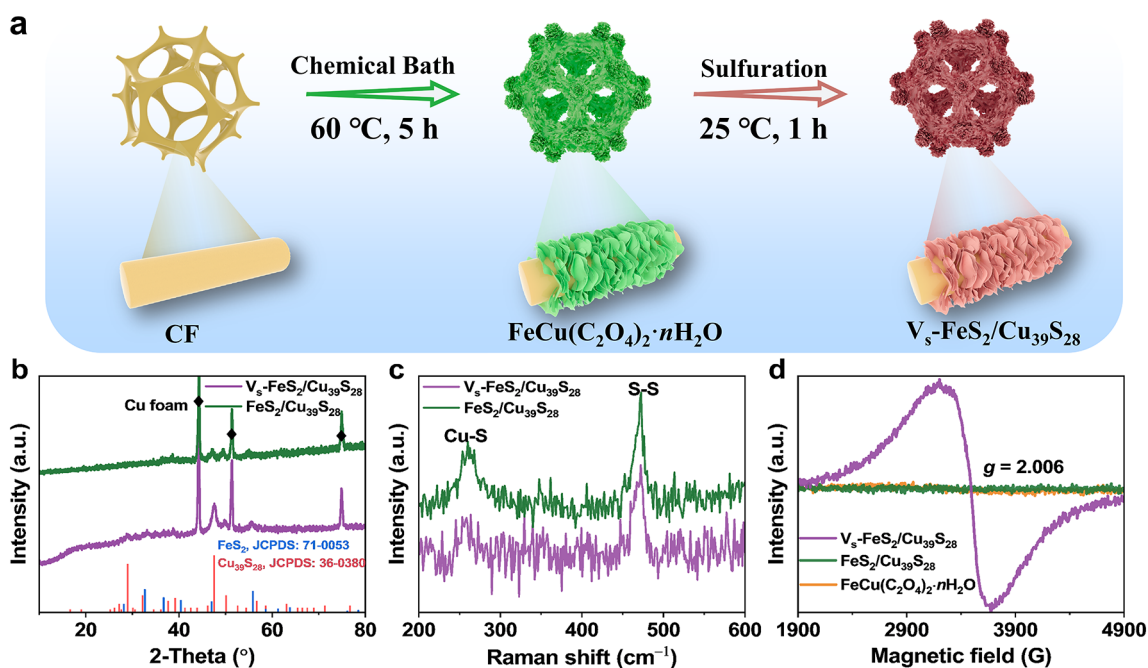


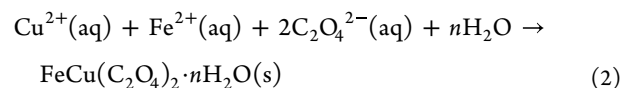
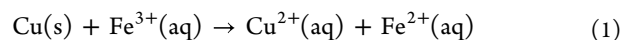
**Figure 1.** (a) Schematic illustration of the preparation of  $\text{V}_s\text{-FeS}_2/\text{Cu}_{39}\text{S}_{28}$ . (b) XRD patterns and (c) Raman spectra of  $\text{V}_s\text{-FeS}_2/\text{Cu}_{39}\text{S}_{28}$  and  $\text{FeS}_2/\text{Cu}_{39}\text{S}_{28}$ . (d) EPR spectra of  $\text{V}_s\text{-FeS}_2/\text{Cu}_{39}\text{S}_{28}$ ,  $\text{FeS}_2/\text{Cu}_{39}\text{S}_{28}$ , and  $\text{FeCu}(\text{C}_2\text{O}_4)_2 \cdot n\text{H}_2\text{O}$ .

sites, modulating the gap states and electronic structure, and optimizing the adsorption free energy of reaction intermediates.<sup>23–25</sup> Evoking cooperative interfacial coupling and defective engineering simultaneously at nanometer coherent interfaces toward enhanced electrocatalysis is of great significance for overall water splitting.<sup>26</sup> Additionally, traditional high-energy synthesis processes and stringent reaction conditions make catalyst scale-up rather uneconomical or difficult. Therefore, developing cost-effective and straightforward methodologies is essential. Corrosion methods for transforming inexpensive metal substrates (e.g., nickel foam, iron foam, and copper foam) into highly active and ultrastable electrodes toward oxygen evolution reaction have been proven to be highly effective.<sup>27,28</sup> The synthetic method was achieved via a redox reaction between metal substrates and anions/cations in an aqueous solution, which is particularly suitable for use under low-energy consumption conditions and endows the material with desirable properties (high catalytic activity and stability).

In this work, we initially propose an innovative strategy involving oxalic acid-assisted vacancy engineering to fabricate a hybrid  $\text{V}_s\text{-FeS}_2/\text{Cu}_{39}\text{S}_{28}$  electrocatalyst. The well-designed electrocatalyst, featuring sulfur vacancies, was successfully grown on CF via facile *in situ* co-precipitation, followed by sulfuration without the provision of excessive energy consumption. The CF used here is directly reacted with the solution and quickly etched without any surfactants, which guarantees deeply anchored contact like a tree rooted in the ground, bolstering its electron transfer capacity and stability.<sup>29</sup> Detailed spectroscopic characterizations substantiate that the synergistic effects between pronounced sulfur vacancies and strategic interfacial coupling can fine-tune the electronic structure for advancing catalytic activity. As anticipated, the resultant  $\text{V}_s\text{-FeS}_2/\text{Cu}_{39}\text{S}_{28}$  showcases low overpotentials of 270 and 370 mV [reversible hydrogen electrode (RHE) (Figure S1)] at 10 and 500  $\text{mA cm}^{-2}$ , respectively, and a small Tafel

slope of 56.4  $\text{mV decade}^{-1}$ , while maintaining exceptional long-term durability in alkaline media. Notably, our crafted two-electrode electrolyzer delivers a low cell voltage of 1.75 V at 100  $\text{mA cm}^{-2}$  along with substantial stability for 80 h, indicating a remarkable potential for the practical application of overall water splitting.

The synthesis of  $\text{V}_s\text{-FeS}_2/\text{Cu}_{39}\text{S}_{28}$  is illustrated schematically in Figure 1a. During the preparation, commercial Cu foam, with high porosity and conductivity, served as both a substrate and a Cu source. Initially,  $\text{FeCu}$  oxalate nanosheets were fabricated through a redox reaction. Theoretically, the standard reduction potential of  $\text{Fe}^{3+}/\text{Fe}^{2+}$  (0.77 V vs RHE) surpasses that of  $\text{Cu}^{2+}/\text{Cu}$  (0.340 V vs RHE).<sup>30,31</sup> Therefore, both  $\text{Cu}^{2+}$  ions dissolved from Cu foam and  $\text{Fe}^{2+}$  ions converted from  $\text{Fe}^{3+}$  react with  $\text{C}_2\text{O}_4^{2-}$  to form metal oxalates by simultaneous dissolution and precipitation, called *in situ* precipitation-induced growth in aqueous (eq 1 and 2).<sup>32</sup> After vulcanization, the precursor quickly changed from verdant green to profound black (Figure S2a).  $\text{FeS}_2/\text{Cu}_{39}\text{S}_{28}$  without oxalic acid as a control experiment was prepared by an identical procedure. Due to the pronouncedly unilateral reaction of  $\text{Fe}^{3+}$  and Cu without  $\text{C}_2\text{O}_4^{2-}$  synchronously involved in precipitation, the Cu substrate in the  $\text{FeS}_2/\text{Cu}_{39}\text{S}_{28}$  catalyst was corroded and became thinner, as shown in Figure S2b.



X-ray diffraction (XRD) elucidated the crystalline structure of as-prepared catalysts. As shown in Figure S3, except for the three strong diffraction peaks attributed to the Cu substrate, other peaks of the precursor are accurately indexed to  $\text{FeC}_2\text{O}_4 \cdot (\text{H}_2\text{O})_2$  (JCPDS Card 72-1305) and  $\text{CuC}_2\text{O}_4 \cdot \text{H}_2\text{O}$  (JCPDS Card 21-0297), evidencing that  $\text{C}_2\text{O}_4^{2-}$  as the anionic ligand

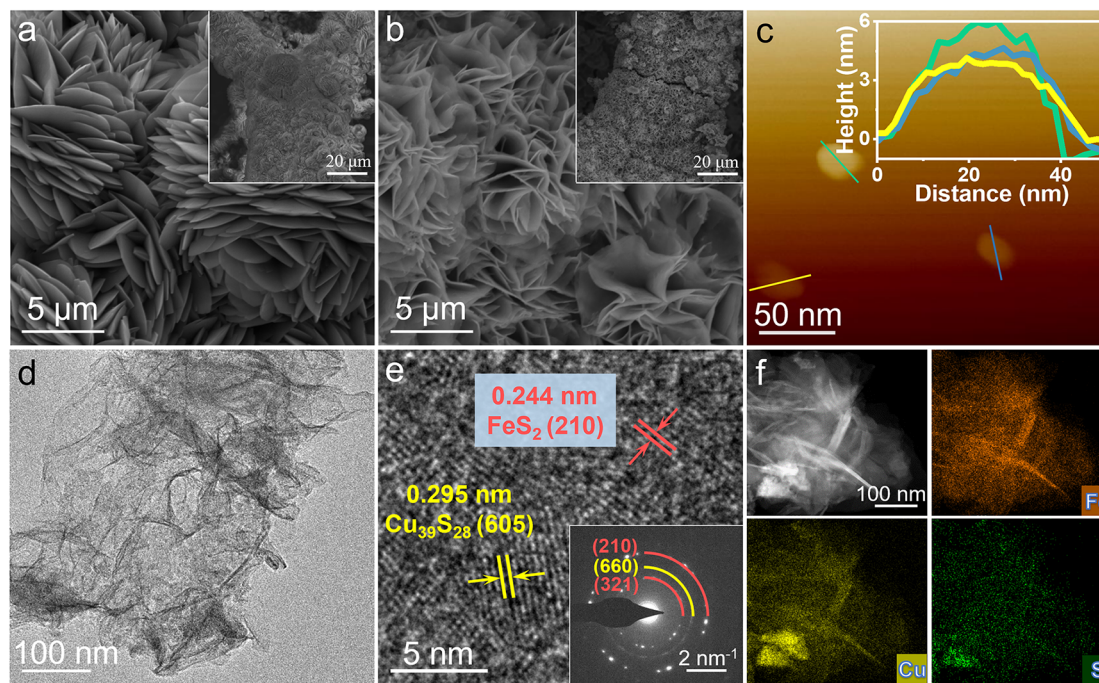


**Figure 2.** SEM images of (a)  $\text{FeCu}(\text{C}_2\text{O}_4)_2 \cdot n\text{H}_2\text{O}$  and (b)  $\text{V}_s\text{-FeS}_2/\text{Cu}_{39}\text{S}_{28}$ . (c) AFM image of the  $\text{V}_s\text{-FeS}_2/\text{Cu}_{39}\text{S}_{28}$  flakes (the inset shows the corresponding line-trace height profile across flakes). (d) TEM and (e) HR-TEM images of  $\text{V}_s\text{-FeS}_2/\text{Cu}_{39}\text{S}_{28}$  (the inset shows the SAED pattern). (f) HAADF-STEM image and corresponding elemental mappings of  $\text{V}_s\text{-FeS}_2/\text{Cu}_{39}\text{S}_{28}$ .

participates in the co-preparation reaction. A similar XRD patterns was obtained for both  $\text{V}_s\text{-FeS}_2/\text{Cu}_{39}\text{S}_{28}$  and  $\text{FeS}_2/\text{Cu}_{39}\text{S}_{28}$  (Figure 1b), demonstrating that oxalic acid treatment has no influence on the phase composition. The distinctive peaks confirm the obtained composite coexistence of  $\text{FeS}_2$  (JCPDS Card 71-0053) and  $\text{Cu}_{39}\text{S}_{28}$  (JCPDS Card 36-0380). Raman spectroscopic measurement was conducted to provide further structural information. Compared with  $\text{V}_s\text{-FeS}_2/\text{Cu}_{39}\text{S}_{28}$  nanosheets,  $\text{FeS}_2/\text{Cu}_{39}\text{S}_{28}$  shows no obvious deviation in Raman spectra. The as-synthesized composites exhibit similar peak widths and characteristic peaks centered at 262 and 470  $\text{cm}^{-1}$ , which represent Raman-active vibrations of the Cu–S and S–S bonds, respectively (Figure 1c).<sup>13</sup> No evident fluctuation is discovered in the electron paramagnetic resonance (EPR) spectrum of  $\text{FeS}_2/\text{Cu}_{39}\text{S}_{28}$ , whereas  $\text{V}_s\text{-FeS}_2/\text{Cu}_{39}\text{S}_{28}$  manifests an obvious paramagnetic absorption signal at  $g = 2.006$ , related to the unpaired electrons of sulfur vacancies (Figure 1d).<sup>33</sup> The generation of sulfur vacancies in  $\text{V}_s\text{-FeS}_2/\text{Cu}_{39}\text{S}_{28}$  is attributed to the introduction of reductive oxalic acid during the synthesis.<sup>34</sup> The intensity of the symmetric peaks is directly proportional to the sulfur vacancy content. Figure S4a shows that the intensity of sulfur vacancies gradually increases along with the increase in the amount of oxalic acid, indicating an increase in sulfur vacancy content. Compared to  $\text{V}_s\text{-FeS}_2$  featuring sulfur vacancies, no vacancy signals are evident in either  $\text{FeS}_2$  or  $\text{Cu}_{39}\text{S}_{28}$ , as Figure S4b can confirm.

The morphological evolution of the  $\text{V}_s\text{-FeS}_2/\text{Cu}_{39}\text{S}_{28}$  composite was tracked by scanning electron microscopy (SEM). As depicted in Figure S5a, commercial CF displays a sleek and unembellished surface.  $\text{FeCu}(\text{C}_2\text{O}_4)_2 \cdot n\text{H}_2\text{O}$ , which blossoms uniformly across the CF, presents a hierarchical hydrangea-like structure composed of intricately stacked nanosheets with a rough yet consistent texture (Figure 2a). Upon vulcanization,  $\text{V}_s\text{-FeS}_2/\text{Cu}_{39}\text{S}_{28}$  exhibits cross-linked

nanosheets covering the surface of the CF substrate (Figure 2b). However,  $\text{FeS}_2/\text{Cu}_{39}\text{S}_{28}$  delineates a distinctly granulated facade, densely populated by solid and protuberant nanoparticles firmly anchored on the CF (Figure S5b), and  $\text{Cu}_{39}\text{S}_{28}$  exhibits a nanoblock morphology. Evidently, the role of oxalic acid transcends mere structural nuances; it is pivotal in executing a meticulous etching operation that invariably produces nanosheets, thus exposing a wealth of active sites. The result of atomic force microscopy (AFM) of the  $\text{V}_s\text{-FeS}_2/\text{Cu}_{39}\text{S}_{28}$  flake prepared by ultrasonic exfoliation from Cu foam in ethanol showcases that the active catalyst shows uniformity at the micro level and filmy characteristics with an average thickness of  $\sim 5$  nm (Figure 2c). We relied on transmission electron microscopy (TEM) to confirm the crystal structure and morphology of  $\text{V}_s\text{-FeS}_2/\text{Cu}_{39}\text{S}_{28}$ . Figure 2d shows the TEM image of the  $\text{V}_s\text{-FeS}_2/\text{Cu}_{39}\text{S}_{28}$  flakes. A high-resolution transmission electron microscopy (HRTEM) image of  $\text{V}_s\text{-FeS}_2/\text{Cu}_{39}\text{S}_{28}$  (Figure 2e) deciphers lattice fringe spacings of 0.244 and 0.295 nm, corresponding to the interplanar distances of (210) and (605) of  $\text{FeS}_2$  and  $\text{Cu}_{39}\text{S}_{28}$ , respectively, which are in agreement with the XRD results. The selected area electron diffraction (SAED) pattern in the inset of Figure 2e exhibits legible diffraction rings of the (210) and (321) planes for  $\text{FeS}_2$  and the (660) plane for  $\text{Cu}_{39}\text{S}_{28}$ . The high-angle annular dark-field (HAADF) TEM image and the corresponding elemental mapping unambiguously indicate the existence and harmonious distribution of Fe, Cu, and S elements across the nanosheets, as shown in Figure 2f. The mass loadings of Fe and S on CF were 3.46 and 1.02  $\text{mg cm}^{-2}$ , respectively [determined by inductively coupled plasma atomic emission spectroscopy (ICP-AES) (Table S1)]. It is noteworthy that, given that Cu serves as both a substrate and a Cu source, the determination of Cu loading is inaccurate. Likewise, the ICP-AES test (Table S1) revealed the detailed elemental loadings of catalysts employing different amounts of oxalic acid.

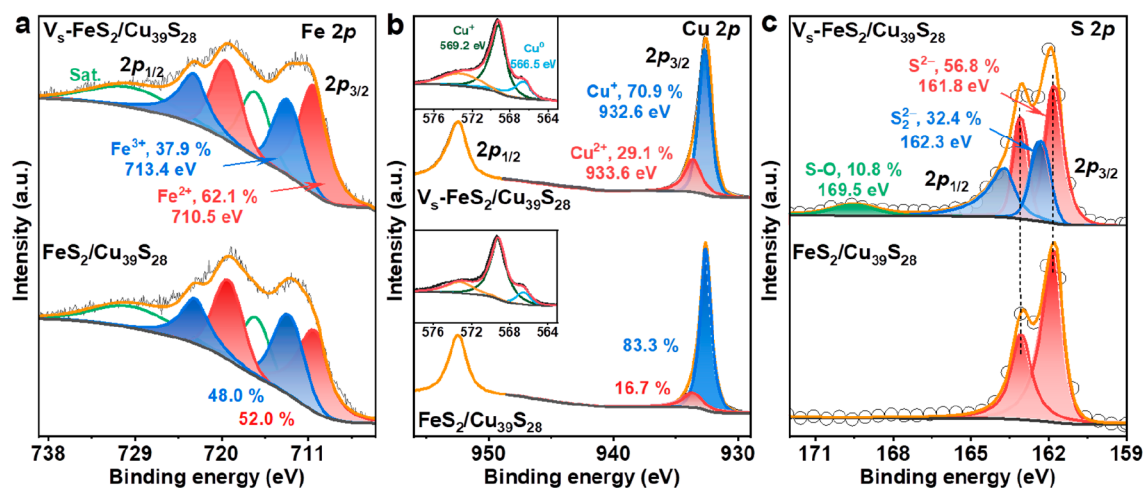


**Figure 3.** High-resolution XPS spectra of (a) Fe 2p, (b) Cu 2p (the inset shows the Cu LMM Auger spectra), and (c) S 2p regions in  $V_s\text{-FeS}_2/\text{Cu}_{39}\text{S}_{28}$  and  $\text{FeS}_2/\text{Cu}_{39}\text{S}_{28}$ .

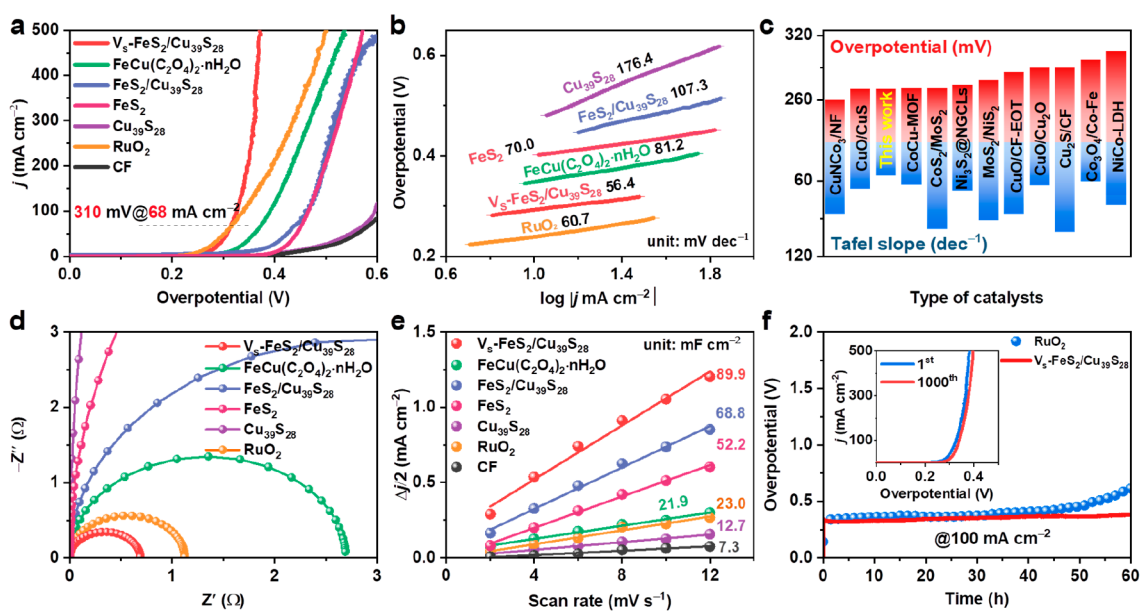


**Figure 4.** Electrochemical OER properties of the catalysts recorded in 1 M KOH. (a) LSV polarization curves and (b) Tafel plots of various catalysts. (c) Comparison of overpotentials at  $10 \text{ mA cm}^{-2}$  and Tafel slopes for previously reported OER catalysts. (d) EIS Nyquist plots. (e) Double-layer capacitance ( $C_{dl}$ ) plots. (f) Chronopotentiometry of  $V_s\text{-FeS}_2/\text{Cu}_{39}\text{S}_{28}$  at  $100 \text{ mA cm}^{-2}$  (the inset shows the polarization curves of  $V_s\text{-FeS}_2/\text{Cu}_{39}\text{S}_{28}$  before and after 1000 cycles).

Surface chemical states and electronic interactions were examined by X-ray photoelectron spectroscopy (XPS). The high-resolution C 1s spectrum of the  $V_s\text{-FeS}_2/\text{Cu}_{39}\text{S}_{28}$  catalyst in Figure S6a is employed as a calibration standard for other elements. The survey spectra (Figure S6b) clearly corroborate the coexistence of Fe, Cu, and S elements in both  $V_s\text{-FeS}_2/\text{Cu}_{39}\text{S}_{28}$  and  $\text{FeS}_2/\text{Cu}_{39}\text{S}_{28}$ . With respect to Fe 2p core level spectra in Figure 3a, the characteristic peaks located at 710.5 and 713.4 eV and that at 716.8 eV can be ascribed to  $\text{Fe}^{2+} 2p_{3/2}$ ,  $\text{Fe}^{3+} 2p_{3/2}$ , and a satellite peak (identified as "Sat."), respectively.<sup>35</sup> A significantly higher percentage of  $\text{Fe}^{2+}$  species ( $\text{Fe}^{2+}/\text{Fe}^{3+}$  ratio of 1.64, calculated the peak fitting area of Fe 2p<sub>3/2</sub>) is observed in the  $V_s\text{-FeS}_2/\text{Cu}_{39}\text{S}_{28}$  electrocatalyst than in  $\text{FeS}_2/\text{Cu}_{39}\text{S}_{28}$  ( $\text{Fe}^{2+}/\text{Fe}^{3+}$  ratio of 1.09) because there are more Fe species with low coordination numbers triggered by the oxalic acid treatment.<sup>36</sup> The deconvoluted Cu 2p spectrum

in Figure 3b clearly shows the strong  $\text{Cu}^+$  or  $\text{Cu}^0 2p_{3/2}$  and  $\text{Cu}^{2+} 2p_{3/2}$  peaks at 932.6 and 933.6 eV, respectively.<sup>37</sup> Given the similar binding energies of the  $\text{Cu}^+$  and  $\text{Cu}^0$  states in the Cu 2p peak, differentiation becomes a challenge.<sup>38</sup> Therefore, further surface state analysis was performed with the Cu LMM Auger peak, as shown in the inset of Figure 3b. In the Cu LMM Auger spectrum, there is a major component at 569.2 eV related to  $\text{Cu}^+$  species and a shoulder at 566.5 eV for  $\text{Cu}^0$  in compounds.<sup>39</sup> Furthermore,  $V_s\text{-FeS}_2/\text{Cu}_{39}\text{S}_{28}$  displays a higher proportion of  $\text{Cu}^{2+}/\text{Cu}^+$  (ratio of 0.41) than of  $\text{FeS}_2/\text{Cu}_{39}\text{S}_{28}$  (ratio of 0.20), evidencing a decrease in the electron density of Cu species. The electrons transfer from  $\text{Cu}_{39}\text{S}_{28}$  to  $\text{FeS}_2$ , further generating an electron-deficient region on  $\text{Cu}_{39}\text{S}_{28}$  and an electron-rich region on  $\text{FeS}_2$ .<sup>40</sup> These results substantiate that reciprocal electronic interaction between  $\text{FeS}_2$  and  $\text{Cu}_{39}\text{S}_{28}$  domains is a primary contributor to the variation percentages,

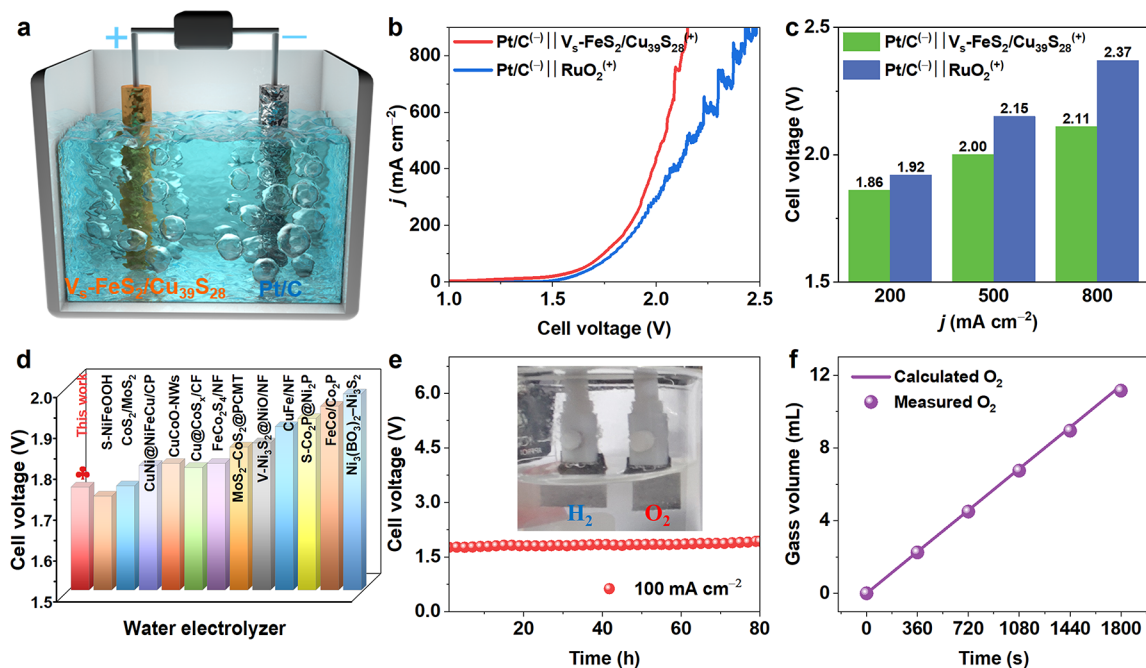


**Figure 5.** Overall water splitting performance of the  $V_s\text{-FeS}_2/\text{Cu}_{39}\text{S}_{28}$  catalyst in 1 M KOH. (a) Schematic description of overall water splitting in a two-electrode system. (b) Polarization curves of the electrolytic cell with  $\text{Pt}/\text{C}^{(-)}||V_s\text{-FeS}_2/\text{Cu}_{39}\text{S}_{28}^{(+)}$  and the reference cell with  $\text{Pt}/\text{C}^{(-)}||\text{RuO}_2^{(+)}$  for overall water splitting. (c) Comparison of the required voltages at current densities of 200, 500, and  $800\text{ mA cm}^{-2}$  of  $\text{Pt}/\text{C}^{(-)}||V_s\text{-FeS}_2/\text{Cu}_{39}\text{S}_{28}^{(+)}$  and  $\text{Pt}/\text{C}^{(-)}||\text{RuO}_2^{(+)}$ . (d) Comparison of the cell voltage at  $100\text{ mA cm}^{-2}$  with those of previously reported catalysts. (e) Chronopotentiometry curves at  $100\text{ mA cm}^{-2}$  of  $\text{Pt}/\text{C}^{(-)}||V_s\text{-FeS}_2/\text{Cu}_{39}\text{S}_{28}^{(+)}$  (the inset shows the experimental phenomenon during a catalyst stability test). (f) Faradaic efficiency for OER.

implying the establishment of coupled interfaces.<sup>41</sup> Such strong interfacial coupling can regulate the electronic structure of a material's surface. Figure 3c compares the S 2p spectra to verify the defective structure. The spectra of  $V_s\text{-FeS}_2/\text{Cu}_{39}\text{S}_{28}$  divulge the contribution from  $\text{S}^{2-}$  ( $2p_{3/2}$  at 161.8 eV),  $\text{S}_2^{2-}$  ( $2p_{3/2}$  at 162.3 eV), and the S–O bond (169.5 eV), in good accordance with the literature.<sup>42</sup> The presence of the oxide is practically unavoidable. Strikingly, for  $\text{FeS}_2/\text{Cu}_{39}\text{S}_{28}$ , devoid of sulfur vacancies, only hallmark peaks of  $\text{S}^{2-}$  can be discovered. For  $V_s\text{-FeS}_2/\text{Cu}_{39}\text{S}_{28}$ , a decrease in the electron cloud density of anions may be attributed to the effect of sulfur vacancies, where the restrained electrons prefer to gravitate toward the surrounding Fe atoms, engendering a higher electron density nearby and leaving the S atoms to be electron-deficient, as evidenced by the emergence of peaks corresponding to  $\text{S}_2^{2-}$  in  $V_s\text{-FeS}_2/\text{Cu}_{39}\text{S}_{28}$ .<sup>43–45</sup>

In brief, XPS analysis reflects alterations in the electronic configuration and possible electron transfer between cations. Furthermore, it demonstrates that strong interfacial coupling between  $\text{FeS}_2$  and  $\text{Cu}_{39}\text{S}_{28}$  constituents may play an important role in modulating the electronic environments of the metal centers, which is favorable for the enhanced catalytic activity.<sup>41,46</sup>

OER performances of as-prepared catalysts were estimated on the basis of the general electrochemical method using a three-electrode configuration in a 1.0 M KOH electrolyte. In addition, the electrochemical data are presented with an  $iR$  correction. From the OER polarization curves exhibited in Figure 4a, to deliver a current density of  $10\text{ mA cm}^{-2}$ , the required overpotential for the  $V_s\text{-FeS}_2/\text{Cu}_{39}\text{S}_{28}$  electrode is 270 mV, surpassing the values of most previously reported Cu-based catalysts (Table S2). Moreover,  $V_s\text{-FeS}_2/\text{Cu}_{39}\text{S}_{28}$  performs noticeably better than  $\text{RuO}_2$  when the current

density exceeds  $68\text{ mA cm}^{-2}$ . Alternatively, a high OER current output of  $500\text{ mA cm}^{-2}$  is secured at a low overpotential of 370 mV, which is more prominent with respect to those of its counterparts. Intriguingly, oxalic acid-treated  $V_s\text{-FeS}_2/\text{Cu}_{39}\text{S}_{28}$  notably outpaces nontreated  $\text{FeS}_2/\text{Cu}_{39}\text{S}_{28}$ , indicating the positive impact of oxalic acid treatment on catalytic activity. The varying amounts of oxalic acid have an impact on the performance. Figure S7a shows that the best OER performance is achieved with 3 mmol of oxalic acid. Compared to the performance of  $\text{FeS}_2$ ,  $V_s\text{-FeS}_2$  exhibits enhanced OER performance, but it is not as good as that of  $V_s\text{-FeS}_2/\text{Cu}_{39}\text{S}_{28}$  (Figure S7b). Additionally, we investigated the influence of different amounts of  $\text{FeCl}_3$  on OER performance. As shown in panels c and d of Figure S7, the LSV curves highlight that the most favorable OER performance is realized on both  $V_s\text{-FeS}_2/\text{Cu}_{39}\text{S}_{28}$  and  $\text{FeS}_2/\text{Cu}_{39}\text{S}_{28}$  with 3 mmol of  $\text{FeCl}_3$ . These results show that the vacancies generated by adding oxalic acid emerge as a dominant factor in the catalytic activity. The electrocatalytic OER mechanisms of  $V_s\text{-FeS}_2/\text{Cu}_{39}\text{S}_{28}$  were examined by constructing Tafel plots, wherein one can see that their slope ( $56.4\text{ mV decade}^{-1}$ ) is smaller than those of  $\text{RuO}_2$  ( $60.7\text{ mV decade}^{-1}$ ),  $\text{FeCu}(\text{C}_2\text{O}_4)_2 \cdot n\text{H}_2\text{O}$  ( $81.2\text{ mV decade}^{-1}$ ),  $\text{FeS}_2/\text{Cu}_{39}\text{S}_{28}$  ( $107.3\text{ mV decade}^{-1}$ ),  $\text{FeS}_2$  ( $70.0\text{ mV decade}^{-1}$ ), and  $\text{Cu}_{39}\text{S}_{28}$  ( $176.4\text{ mV decade}^{-1}$ ) (Figure 4b). Normally, the smaller Tafel slope signifies more advantageous reaction kinetics.<sup>47</sup> Videlicet,  $V_s\text{-FeS}_2/\text{Cu}_{39}\text{S}_{28}$  possesses the fastest OER reaction kinetics among the aforementioned electrocatalysts. Noteworthy,  $V_s\text{-FeS}_2/\text{Cu}_{39}\text{S}_{28}$  is comparable to other representative non-precious metal catalysts recently reported in terms of both OER overpotential and Tafel slope, as presented in Figure 4c and Table S2.

Electrochemical impedance spectroscopy (EIS) analysis is depicted in Figure 4d, where the arcs represent a positive

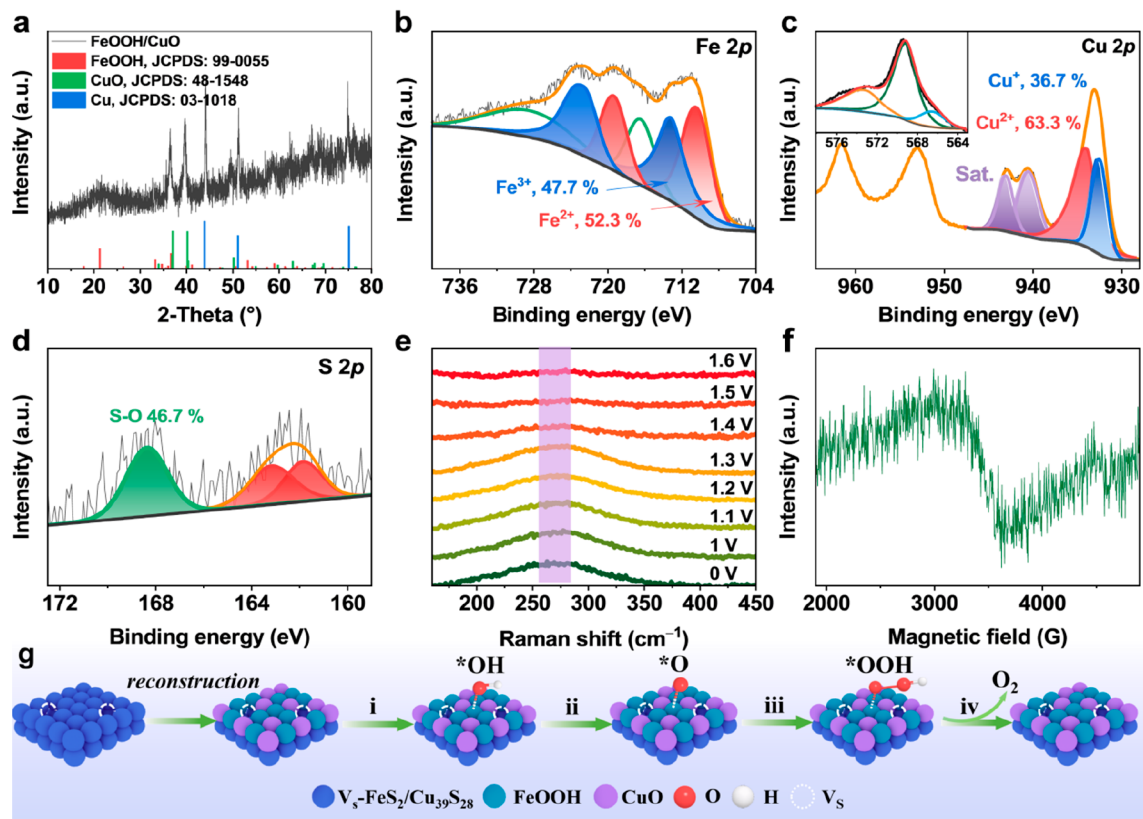


**Figure 6.** (a) XRD pattern and (b) Fe 2p, (c) Cu 2p (the inset shows Cu LMM Auger spectra), and (d) S 2p XPS spectra of  $V_s$ -FeS<sub>2</sub>/Cu<sub>39</sub>S<sub>28</sub> after the OER durability test. (e) *In situ* Raman spectra of  $V_s$ -FeS<sub>2</sub>/Cu<sub>39</sub>S<sub>28</sub>. (f) EPR spectra of  $V_s$ -FeS<sub>2</sub>/Cu<sub>39</sub>S<sub>28</sub> after the OER durability test. (g) Schematic illustration of the OER of  $V_s$ -FeS<sub>2</sub>/Cu<sub>39</sub>S<sub>28</sub>.

correlation with the charge transfer resistance ( $R_{ct}$ ). This reveals that the charge transfer resistance ( $R_{ct} = 0.6 \Omega$ ) of the  $V_s$ -FeS<sub>2</sub>/Cu<sub>39</sub>S<sub>28</sub> catalyst is lower than that of the other reference sample, leading to a faster reaction kinetics for OER. To further assess intrinsic activity, the electrochemical double-layer capacitance ( $C_{dl}$ ) values were then evaluated to uncover the actual quantities of active sites of electrocatalysts, which is proportional to the electrochemical surface area (ECSA). The ECSA (1498.3 cm<sup>2</sup>) estimated from the  $C_{dl}$  (89.9 mF cm<sup>-2</sup>) of  $V_s$ -FeS<sub>2</sub>/Cu<sub>39</sub>S<sub>28</sub> unequivocally confirms highly exposed active sites following oxalic acid treatment (Figure 4e and Figures S7 and S8). Moreover, the synergistic effect of monophasic FeS<sub>2</sub> and Cu<sub>39</sub>S<sub>28</sub> also augments the intrinsic activity. The stability of  $V_s$ -FeS<sub>2</sub>/Cu<sub>39</sub>S<sub>28</sub> was evaluated by chronopotentiometry (CP) tests at the current density of 100 mA cm<sup>-2</sup>. As illustrated in Figure 4f, compared with the RuO<sub>2</sub> catalyst,  $V_s$ -FeS<sub>2</sub>/Cu<sub>39</sub>S<sub>28</sub> exhibited imperceptible attenuation in the electrolytic OER test for 60 h, further corroborating its preeminent durability under alkaline conditions. Furthermore, the inset of Figure 4f shows that the OER performance of  $V_s$ -FeS<sub>2</sub>/Cu<sub>39</sub>S<sub>28</sub> is well maintained after 1000 CV scans without conspicuous variation in the LSV curves. The slight potential shift may be attributed to the catalyst exhibiting mild aggregation in morphology after experiencing oxidation–reduction reactions (Figure S11a).

The summarized OER catalytic parameters of different catalysts in a 1.0 M KOH solution (Table S3) crisply substantiate the overwhelming activity of target catalyst  $V_s$ -FeS<sub>2</sub>/Cu<sub>39</sub>S<sub>28</sub>. By comparing with monophasic counterparts and flawless FeS<sub>2</sub>/Cu<sub>39</sub>S<sub>28</sub>,  $V_s$ -FeS<sub>2</sub>/Cu<sub>39</sub>S<sub>28</sub> during alkaline

OER progress achieves dramatically enhanced OER activity. In essence, the implanted distinct sulfur vacancies, heightened electronic interaction, and nanosheet structure amplify not only the active site exposure and electrical transport properties but also the intrinsic catalyst activity of  $V_s$ -FeS<sub>2</sub>/Cu<sub>39</sub>S<sub>28</sub>.<sup>48</sup>

Bearing such remarkable OER properties for the  $V_s$ -FeS<sub>2</sub>/Cu<sub>39</sub>S<sub>28</sub> catalyst, a two-electrode system was constructed to explore the overall water splitting activity. In a 1.0 M KOH solution,  $V_s$ -FeS<sub>2</sub>/Cu<sub>39</sub>S<sub>28</sub> served as the anode and commercial Pt/C as the cathode [denoted as Pt/C<sup>(-)</sup>|| $V_s$ -FeS<sub>2</sub>/Cu<sub>39</sub>S<sub>28</sub><sup>(+)</sup>], as shown in Figure 5a. For comparison, a reference electrolyzer was also assembled by using the RuO<sub>2</sub> and Pt/C catalysts loaded on CF as the anode and cathode, respectively [denoted as Pt/C<sup>(-)</sup>||RuO<sub>2</sub><sup>(+)</sup>]. According to the LSV curve in Figure 5b, the cell with Pt/C<sup>(-)</sup>|| $V_s$ -FeS<sub>2</sub>/Cu<sub>39</sub>S<sub>28</sub><sup>(+)</sup>-coupled electrodes operated at cell voltages of 1.54 V to reach a current density of 10 mA cm<sup>-2</sup>, superior to that of the reference cell with Pt/C<sup>(-)</sup>||RuO<sub>2</sub><sup>(+)</sup>. The electrolysis voltages at various current densities are summarized in Figure 5c, and Pt/C<sup>(-)</sup>|| $V_s$ -FeS<sub>2</sub>/Cu<sub>39</sub>S<sub>28</sub><sup>(+)</sup> afforded a lower cell voltage to reach current densities of 200, 500, and 800 mA cm<sup>-2</sup>. As profiled in Figure 5d and Table S4, our cell performance at a high current density (1.75 V at 100 mA cm<sup>-2</sup>) is substantially competitive among the noble metal-free electrocatalysts reported in the literature. Moreover, the cell with Pt/C<sup>(-)</sup>|| $V_s$ -FeS<sub>2</sub>/Cu<sub>39</sub>S<sub>28</sub><sup>(+)</sup>-coupled electrodes remains stable during 80 h of continuous operation at a current density of 100 mA cm<sup>-2</sup>, elucidating its remarkable stability, as shown in Figure 5e. In short,  $V_s$ -FeS<sub>2</sub>/Cu<sub>39</sub>S<sub>28</sub> emerges as a compelling anode material for electrocatalytic water oxidation. Meanwhile, continuous effervescence is

observed at the anode, corroborating the evolution of  $O_2$ . Furthermore, the Faradaic efficiency (FE) of the OER process, representing the ratio of actual gas evolved to the theoretically expected amount, was calculated. Initially, the theoretical volume of the expected total gas was evaluated using Faraday's law of electrolysis with the ideal gas law. The evolved gas volume of  $O_2$  was measured through the drainage method.  $V_s$ - $FeS_2/Cu_{39}S_{28}$  exhibits nearly 100% Faradaic efficiency of  $O_2$  production at a current density of  $100 \text{ mA cm}^{-2}$  (Figure Sf and Figure S9), indicating a high energy conversion rate in the electrocatalytic reaction.

We further investigate the reconfiguration of the heterostructure during the OER process, as the sulfides are known as precatalysts that would be inevitably oxidized and converted to their homologous oxides/(oxy)hydroxides on the surfaces under oxidizing potentials. These entities are the major contributor to the OER activity.<sup>42,49</sup> This point is further confirmed by combined post-XRD (Figure 6a) and post-XPS (Figure 6b–d) over the  $V_s$ - $FeS_2/Cu_{39}S_{28}$  electrocatalyst after the CP measurement. These reveal that  $V_s$ - $FeS_2/Cu_{39}S_{28}$  was transformed into the corresponding (oxy)hydroxide and oxide, consistent with prior studies.<sup>50–52</sup> As depicted in Figure 6b, the intensity of  $Fe^{3+}$  species in the Fe 2p spectra increases after the OER, implying the possibility of formation of  $FeOOH$ , which can serve as the active phase to further boost the OER performance. Similar characteristics can be observed in the Cu 2p spectra (Figure 6c). Additionally, the peak intensities of S 2p<sub>1/2</sub> and S 2p<sub>3/2</sub> spectra notably decrease, accompanied by the enlargement of the S–O bonds (Figure 6d), revealing the conversion of metal sulfides to metal oxides or hydroxides during the catalytic process. Simultaneously, *in situ* Raman spectroscopy further dynamically monitors the progressive weakening of Cu–S bonds as the potential increases, indicating a phase transformation of Cu–S (Figure 6e). It is noteworthy that *in situ* Raman reveals a clear distinction of the electrode after immersion in an alkaline electrolyte compared to its dry state, which may be attributed to the weakening of the Raman scattering peak at  $470 \text{ cm}^{-1}$  in a humid environment. Furthermore, post-SEM (Figure S11b) indicates slight agglomeration on the surface morphology. As proven in Figure 6f, EPR spectra also reveal that sulfur vacancies still exist in  $V_s$ - $FeS_2/Cu_{39}S_{28}$  after the OER. These results collectively demonstrate that the catalyst's surfaces undergo structural transformation to form metal oxyhydroxides during the OER.

Generally, the mechanism of the OER in an alkaline solution involves a four-electron transfer process and three intermediates ( $OH^*$ ,  $O^*$ , and  $OOH^*$ ) on the active site. For the  $V_s$ - $FeS_2/Cu_{39}S_{28}$  electrocatalyst, a proposed reaction scheme for surface reconstruction is delineated in Figure 6g; parts of the  $FeS_2$  and  $Cu_{39}S_{28}$  components will be initially oxidized to their homologous oxides/(oxy)hydroxides during the OER, which create the contact between the  $FeS_2$  and  $Cu_{39}S_{28}$  components.<sup>53</sup> The underlying sulfide substrate enables not only interface coupling with the actual active site species on the surface but also efficient electron transport in the inner layer, further exhibiting a high intrinsic OER activity. The *in situ*-generated  $FeOOH$  shell provides abundant active sites for the OER, while the participation of Cu species effectively enhanced the OER catalytic activity at Fe sites of  $V_s$ - $FeS_2/Cu_{39}S_{28}$ . Density functional theory (DFT) calculations by Zhang et al. have confirmed that the Gibbs free energy ( $\Delta G$ ) of the  $* + H_2O \rightarrow OH^*$  reaction is significantly reduced with the assistance of Cu species, demonstrating the more obviously

thermodynamically favored catalytic reaction step.<sup>19</sup> Overall, the synergy from the complementary functions of multiple active sites contributes to the overall activity. Except for multicomponent synergies, the introduction of a vacancy emerges as a potent tool for refining the electrocatalytic competencies. On the contrary, after the formation of a sulfur vacancy in  $V_s$ - $FeS_2/Cu_{39}S_{28}$ , the defect site suffers from strong electron depletion, favoring the absorption of negatively charged  $OH^-$  in an alkaline electrolyte at the defect site and facilitating the subsequent OER.<sup>54</sup> Sun et al. observed that construction of sulfur vacancies in  $Fe-Ni_3S_2$ , led to the optimized binding energy of the intermediate and reduced reaction barrier of the rate-determining step.<sup>55</sup> On the contrary, vacancies enforced the electronic interactions between  $FeS_2$  and  $Cu_{39}S_{28}$  constituents, favorable for the enhanced catalytic activity. In addition, theoretical considerations suggest that vacancies strengthen the density of states near the Fermi level, exhibiting higher electronic conductivity.<sup>45</sup> It is consistent with the EIS results showing that the charge transfer resistance ( $R_{ct}$ ) of  $V_s$ - $FeS_2/Cu_{39}S_{28}$  with a vacancy is smaller than that of  $FeS_2/Cu_{39}S_{28}$ . The incorporation of sulfur vacancies plays an important role in boosting catalytic performance in general.

The outstanding OER electrocatalytic activity and stability as well as the excellent overall water splitting performance of the  $V_s$ - $FeS_2/Cu_{39}S_{28}$  catalyst are also associated with the following factors. (1) The sulfur vacancy refines the catalyst's electronic properties and amplifies the intrinsic activity of active sites. (2) The nanosheet structure is conducive to a high density of active sites and acceleration of mass transport. (3) The high conductivity of the self-supporting electrode can be favorable for electron transfer. These factors demonstrate the active origin of  $V_s$ - $FeS_2/Cu_{39}S_{28}$ ; its advantages mentioned above are considered to be the key to improving electrocatalytic performance.

In summary, we have developed the  $V_s$ - $FeS_2/Cu_{39}S_{28}$  nanocomposite with sulfur vacancies through *in situ* coprecipitation growth and subsequent vulcanization. The achieved  $V_s$ - $FeS_2/Cu_{39}S_{28}$  displays remarkable OER activity with a low overpotential of 370 mV at  $500 \text{ mA cm}^{-2}$  and robust stability for 60 h at  $100 \text{ mA cm}^{-2}$ , outperforming the majority of Cu-based electrocatalysts. The catalyst was further used in an alkaline electrolyzer, achieving  $100 \text{ mA cm}^{-2}$  at a cell voltage of 1.75 V and exceptional durability for 80 h. The strong coupling effects between  $FeS_2$  and  $Cu_{39}S_{28}$  and distinct vacancy defects can supply sufficient exposure of active sites and enhance electrical transport properties, being responsible for its eminent performance. This work not only introduces a low-cost and potent Cu-based electrocatalyst but also broadens the horizons for employing non-precious metals in the pivotal process of water oxidation.

## ■ ASSOCIATED CONTENT

### Supporting Information

The Supporting Information is available free of charge at <https://pubs.acs.org/doi/10.1021/acs.jpcllett.3c03256>.

Details of the materials, synthesis procedures, characterization, electrochemical measurements, impedance spectroscopy study, and a comparison of OERs (PDF)

## AUTHOR INFORMATION

## Corresponding Authors

**Xiulin Yang** – Guangxi Key Laboratory of Low Carbon Energy Materials, School of Chemistry and Pharmaceutical Sciences, Guangxi Normal University, Guilin 541004 Guangxi, China; [orcid.org/0000-0003-2642-4963](https://orcid.org/0000-0003-2642-4963); Email: [xlyang@gxnu.edu.cn](mailto:xlyang@gxnu.edu.cn)

**Tayirjan Taylor Isimjan** – Saudi Arabia Basic Industries Corporation (SABIC) at King Abdullah University of Science and Technology (KAUST), Thuwal 23955-6900, Saudi Arabia; [orcid.org/0000-0003-1735-481X](https://orcid.org/0000-0003-1735-481X); Email: [isimjant@sabic.com](mailto:isimjant@sabic.com)

## Authors

**Fengli Wei** – Guangxi Key Laboratory of Low Carbon Energy Materials, School of Chemistry and Pharmaceutical Sciences, Guangxi Normal University, Guilin 541004 Guangxi, China

**Jinghao Shen** – Guangxi Key Laboratory of Low Carbon Energy Materials, School of Chemistry and Pharmaceutical Sciences, Guangxi Normal University, Guilin 541004 Guangxi, China

**Junlin Gong** – Guangxi Key Laboratory of Low Carbon Energy Materials, School of Chemistry and Pharmaceutical Sciences, Guangxi Normal University, Guilin 541004 Guangxi, China

**Qimin Peng** – Guangxi Key Laboratory of Low Carbon Energy Materials, School of Chemistry and Pharmaceutical Sciences, Guangxi Normal University, Guilin 541004 Guangxi, China

**Luyan Shi** – Guangxi Key Laboratory of Low Carbon Energy Materials, School of Chemistry and Pharmaceutical Sciences, Guangxi Normal University, Guilin 541004 Guangxi, China

Complete contact information is available at:

<https://pubs.acs.org/10.1021/acs.jpcl.3c03256>

## Notes

The authors declare no competing financial interest.

## ACKNOWLEDGMENTS

This work was supported by the National Natural Science Foundation of China (21965005 and 52363028), the Natural Science Foundation of Guangxi Province (2021GXNSFAA076001), and the Guangxi Technology Base and Talent Subject (GUIKE AD18126001 and GUIKE AD20297039).

## REFERENCES

- (1) Yu, Z. Y.; Duan, Y.; Kong, Y.; Zhang, X. L.; Feng, X. Y.; Chen, Y.; Wang, H.; Yu, X.; Ma, T.; Zheng, X.; et al. General Synthesis of Tube-Like Nanostructured Perovskite Oxides with Tunable Transition Metal-Oxygen Covalency for Efficient Water Electrooxidation in Neutral Media. *J. Am. Chem. Soc.* **2022**, *144*, 13163.
- (2) Li, H.; Chen, S.; Zhang, Y.; Zhang, Q.; Jia, X.; Zhang, Q.; Gu, L.; Sun, X.; Song, L.; Wang, X. Systematic Design of Superaerophobic Nanotube-Array Electrode Comprised of Transition-Metal Sulfides for Overall Water Splitting. *Nat. Commun.* **2018**, *9*, 2452.
- (3) Ye, S.-H.; Shi, Z.-X.; Feng, J.-X.; Tong, Y.-X.; Li, G.-R. Activating CoOOH Porous Nanosheet Arrays by Partial Iron Substitution for Efficient Oxygen Evolution Reaction. *Angew. Chem., Int. Ed.* **2018**, *57*, 2672.
- (4) Bai, Y.; Wu, Y.; Zhou, X.; Ye, Y.; Nie, K.; Wang, J.; Xie, M.; Zhang, Z.; Liu, Z.; Cheng, T.; et al. Promoting Nickel Oxidation State Transitions in Single-Layer NiFeB Hydroxide Nanosheets for Efficient Oxygen Evolution. *Nat. Commun.* **2022**, *13*, 6094.
- (5) Seh, Z. W.; Kibsgaard, J.; Dickens, C. F.; Chorkendorff, J.; Nørskov, J. K.; Jaramillo, T. F. Combining Theory and Experiment in Electrocatalysis: Insights into Materials Design. *Science* **2017**, *355*, No. eaad4998.
- (6) Wang, L.; Hao, Y.; Deng, L.; Hu, F.; Zhao, S.; Li, L.; Peng, S. Rapid complete reconfiguration induced actual active species for industrial hydrogen evolution reaction. *Nat. Commun.* **2022**, *13*, 5785.
- (7) Yin, J.; Jin, J.; Lin, H.; Yin, Z.; Li, J.; Lu, M.; Guo, L.; Xi, P.; Tang, Y.; Yan, C.-H. Optimized Metal Chalcogenides for Boosting Water Splitting. *Adv. Sci.* **2020**, *7*, No. 1903070.
- (8) Xu, X.; Cao, A.; You, W.; Tao, Z.; Kang, L.; Liu, J. Assembly of Cobalt Layered Double Hydroxide on Cuprous Phosphide Nanowire with Strong Built-In Potential for Accelerated Overall Water Splitting. *Small* **2021**, *17*, No. 2101725.
- (9) Ren, X.; Ji, X.; Wei, Y.; Wu, D.; Zhang, Y.; Ma, M.; Liu, Z.; Asiri, A. M.; Wei, Q.; Sun, X. In Situ Electrochemical Development of Copper Oxide Nanocatalysts within a TCNQ Nanowire Array: A Highly Conductive Electrocatalyst for the Oxygen Evolution Reaction. *Chem. Commun.* **2018**, *54*, 1425.
- (10) Gu, M.; Jiang, L.; Zhao, S.; Wang, H.; Lin, M.; Deng, X.; Huang, X.; Gao, A.; Liu, X.; Sun, P.; et al. Deciphering the Space Charge Effect of the p-n Junction between Copper Sulfides and Molybdenum Selenides for Efficient Water Electrolysis in a Wide pH Range. *ACS Nano* **2022**, *16*, 15425.
- (11) Chen, J.; Gu, M.; Liu, S.; Sheng, T.; Zhang, X. Iron Doped in the Subsurface of CuS Nanosheets by Interionic Redox: Highly Efficient Electrocatalysts toward the Oxygen Evolution Reaction. *ACS Appl. Mater. Interfaces* **2021**, *13*, 16210–16217.
- (12) Chen, N.; Wang, Y.; Du, X.; Zhang, X. Facile Fabrication of Flower-like CuS/MnCO<sub>3</sub> Microspheres Clusters on Nickel Foam as an Efficient Bifunctional Catalyst for Overall Water Splitting. *Int. J. Hydrogen Energy* **2021**, *46*, 19948–19961.
- (13) Zhu, J.; Zi, S.; Zhang, N.; Hu, Y.; An, L.; Xi, P. Surface Reconstruction of Covellite CuS Nanocrystals for Enhanced OER Catalytic Performance in Alkaline Solution. *Small* **2023**, *19*, No. 2301762.
- (14) Kale, S. B.; Babar, P. T.; Kim, J.-H.; Lokhande, C. D. Synthesis of One Dimensional Cu<sub>2</sub>S Nanorods Using a Self-Grown Sacrificial Template for the Electrocatalytic Oxygen Evolution Reaction (OER). *New J. Chem.* **2020**, *44*, 8771.
- (15) Zhao, G.; Li, P.; Cheng, N.; Dou, S. X.; Sun, W. An Ir/Ni(OH)<sub>2</sub> Heterostructured Electrocatalyst for the Oxygen Evolution Reaction: Breaking the Scaling Relation, Stabilizing Iridium(V), and Beyond. *Adv. Mater.* **2020**, *32*, No. 2000872.
- (16) Wang, B.; Chen, Y.; Liu, G.; Liu, D.; Liu, Y.; Ge, C.; Wang, L.; Wang, Z.; Wu, R.; Wang, L. Interfaces Coupling of Co<sub>8</sub>FeS<sub>8</sub>-Fe<sub>3</sub>C<sub>2</sub> with Elevated d-Band Center for Efficient Water Oxidation Catalysis. *Appl. Catal. B: Environ.* **2024**, *341*, No. 123294.
- (17) Fei, B.; Chen, Z.; Liu, J.; Xu, H.; Yan, X.; Qing, H.; Chen, M.; Wu, R. Ultrathinning Nickel Sulfide with Modulated Electron Density for Efficient Water Splitting. *Adv. Energy Mater.* **2020**, *10*, No. 2001963.
- (18) Xu, J.; Cui, J.; Guo, C.; Zhao, Z.; Jiang, R.; Xu, S.; Zhuang, Z.; Huang, Y.; Wang, L.; Li, Y. Ultrasmall Cu<sub>7</sub>S<sub>4</sub>@MoS<sub>2</sub> Hetero-Nanoframes with Abundant Active Edge Sites for Ultrahigh-Performance Hydrogen Evolution. *Angew. Chem., Int. Ed.* **2016**, *55*, 6502.
- (19) Zhang, N.; Gao, Y.; Mei, Y.; Liu, J.; Song, W.; Yu, Y. CuS-Ni<sub>3</sub>S<sub>2</sub> Grown *in situ* from Three-Dimensional Porous Bimetallic Foam for Efficient Oxygen Evolution. *Inorg. Chem. Front.* **2019**, *6*, 293.
- (20) Xiao, Y.; Shen, Y.; Su, D.; Zhang, S.; Yang, J.; Yan, D.; Fang, S.; Wang, X. Engineering Cu<sub>1.96</sub>S/Co<sub>9</sub>S<sub>8</sub> with Sulfur Vacancy and Heterostructure as an Efficient Bifunctional Electrocatalyst for Water Splitting. *J. Mater. Sci. Technol.* **2023**, *154*, 1.
- (21) Zou, X.; Wu, Y.; Liu, Y.; Liu, D.; Li, W.; Gu, L.; Liu, H.; Wang, P.; Sun, L.; Zhang, Y. In Situ Generation of Bifunctional, Efficient Fe-Based Catalysts from Mackinawite Iron Sulfide for Water Splitting. *Chem.* **2018**, *4*, 1139–1152.

- (22) Guo, B.; Huo, H.; Zhuang, Q.; Ren, X.; Wen, X.; Yang, B.; Huang, X.; Chang, Q.; Li, S. Iron Oxyhydroxide: Structure and Applications in Electrocatalytic Oxygen Evolution Reaction. *Adv. Funct. Mater.* **2023**, *33*, No. 2300557.
- (23) Huang, Z.; Liu, Z.; Liao, M.; Wang, L.; Luo, Z.; Isimjan, T. T.; Yang, X. Synergistically Improved Hydrogen Evolution by Interface Engineering of Monodispersed  $\text{Co}_{5.47}\text{N}/\text{CoMoO}_x$  Hybrid Particles on Carbon Cloth with Rich Oxygen Vacancies. *Chem. Eng. J.* **2023**, *462*, No. 142281.
- (24) Zhang, Y.; Lu, R.; Wang, C.; Zhao, Y.; Qi, L. Electronic and Vacancy Engineering of Mo–RuCoO<sub>x</sub> Nanoarrays for High-Efficiency Water Splitting. *Adv. Funct. Mater.* **2023**, *33*, No. 2303073.
- (25) Ye, Z.; Jiang, Y.; Li, L.; Wu, F.; Chen, R. Synergetic Anion Vacancies and Dense Heterointerfaces into Bimetal Chalcogenide Nanosheet Arrays for Boosting Electrocatalysis Sulfur Conversion. *Adv. Mater.* **2022**, *34*, No. 2109552.
- (26) Yang, H.; Liu, J.; Chen, Z.; Wang, R.; Fei, B.; Liu, H.; Guo, Y.; Wu, R. Unconventional Bi-Vacancies Activating Inert Prussian Blue Analogues Nanocubes for Efficient Hydrogen Evolution. *Chem. Eng. J.* **2021**, *420*, No. 127671.
- (27) Liu, Y.; Liang, X.; Gu, L.; Zhang, Y.; Li, G.-D.; Zou, X.; Chen, J.-S. Corrosion Engineering towards Efficient Oxygen Evolution Electrodes with Stable Catalytic Activity for over 6000 h. *Nat. Commun.* **2018**, *9*, 2609.
- (28) Li, Z.; Yao, Y.; Sun, S.; Liang, J.; Hong, S.; Zhang, H.; Yang, C.; Zhang, X.; Cai, Z.; Li, J.; et al. Carbon Oxyanion Self-Transformation on NiFe Oxalates Enables Long-Term Ampere-Level Current Density Seawater Oxidation. *Angew. Chem., Int. Ed.* **2024**, *63*, No. e202316522.
- (29) Yu, L.; Wu, L.; McElhenny, B.; Song, S.; Luo, D.; Zhang, F.; Yu, Y.; Chen, S.; Ren, Z. Ultrafast Room-temperature Synthesis of Porous S-doped Ni/Fe (Oxy)hydroxide Electrodes for Oxygen Evolution Catalysis in Seawater Splitting. *Energy Environ. Sci.* **2020**, *13*, 3439.
- (30) Ha, J.; Kim, M.; Kim, Y.-T.; Choi, J. Ni<sub>0.67</sub>Fe<sub>0.33</sub> Hydroxide Incorporated with Oxalate for Highly Efficient Oxygen Evolution Reaction. *ACS Appl. Mater. Interfaces* **2021**, *13*, 42870.
- (31) Liu, F.; Peng, C.; Wilson, B. P.; Lundström, M. Oxalic Acid Recovery from High Iron Oxalate Waste Solution by a Combination of Ultrasound-Assisted Conversion and Cooling Crystallization. *ACS Sustain. Chem. Eng.* **2019**, *7*, 17372.
- (32) Ha, J.; Kim, Y.-T.; Choi, J. In Situ Precipitation-Induced Growth of Leaf-Like CuO Nanostructures on Cu–Ni Alloys for Binder-Free Anodes in Li-Ion Batteries. *ChemSusChem* **2020**, *13*, 419.
- (33) Pang, Q.-Q.; Niu, Z.-L.; Yi, S.-S.; Zhang, S.; Liu, Z.-Y.; Yue, X.-Z. Hydrogen-Etched Bifunctional Sulfur-Defect-Rich  $\text{ReS}_2/\text{CC}$  Electrode for Highly Efficient HER and OER. *Small* **2020**, *16*, No. 2003007.
- (34) Yang, J.; Hu, S.; Shi, L.; Hoang, S.; Yang, W.; Fang, Y.; Liang, Z.; Pan, C.; Zhu, Y.; Li, L.; et al. Oxygen Vacancies and Lewis Acid Sites Synergistically Promoted Catalytic Methane Combustion over Perovskite Oxides. *Environ. Sci. Technol.* **2021**, *55*, 9243–9254.
- (35) Lyu, S.; Guo, C.; Wang, J.; Li, Z.; Yang, B.; Lei, L.; Wang, L.; Xiao, J.; Zhang, T.; Hou, Y. Exceptional Catalytic Activity of Oxygen Evolution Reaction via Two-Dimensional Graphene Multilayer Confined Metal–Organic Frameworks. *Nat. Commun.* **2022**, *13*, 6171.
- (36) Zhao, Y.; Luo, Y.; Sun, B.; Li, T.; Han, S.; Dong, X.; Lin, H. Rational Construction of Reduced  $\text{NiCo}_2\text{S}_4@/\text{CuCo}_2\text{S}_4$  Composites with Sulfur Vacancies as High-performance Supercapacitor Electrode for Enhancing Electrochemical Energy Storage. *Compos. Part B Eng.* **2022**, *243*, No. 110088.
- (37) Guo, M.; Huang, Z.; Qu, Y.; Wang, L.; Li, H.; Isimjan, T. T.; Yang, X. Synergistic Effect and Nanostructure Engineering of Three-Dimensionally Hollow Mesoporous Spherical  $\text{Cu}_3\text{P}/\text{TiO}_2$  in Aqueous/Flexible Zn–Air Batteries. *Appl. Catal. B Environ.* **2023**, *320*, No. 121991.
- (38) Lee, S. Y.; Jung, H.; Kim, N.-K.; Oh, H.-S.; Min, B. K.; Hwang, Y. J. Mixed Copper States in Anodized Cu Electrocatalyst for Stable and Selective Ethylene Production from CO<sub>2</sub> Reduction. *J. Am. Chem. Soc.* **2018**, *140*, 8681.
- (39) Qu, M.; Zhang, F. Q.; Wang, D. H.; Li, H.; Hou, J. J.; Zhang, X. M. Observation of Non-FCC Copper in Alkynyl-Protected Cu<sub>53</sub> Nanoclusters. *Angew. Chem., Int. Ed.* **2020**, *59*, 6507.
- (40) Yang, Y.; Dai, Q.; Shi, L.; Liu, Y.; Isimjan, T. T.; Yang, X. Electronic Modulation of Pt Nanoparticles on Ni<sub>3</sub>N–Mo<sub>2</sub>C by Support-Induced Strategy for Accelerating Hydrogen Oxidation and Evolution. *J. Phys. Chem. Lett.* **2022**, *13*, 2107.
- (41) An, L.; Li, Y.; Luo, M.; Yin, J.; Zhao, Y.-Q.; Xu, C.; Cheng, F.; Yang, Y.; Xi, P.; Guo, S. Atomic-Level Coupled Interfaces and Lattice Distortion on CuS/NiS<sub>2</sub> Nanocrystals Boost Oxygen Catalysis for Flexible Zn–Air Batteries. *Adv. Funct. Mater.* **2017**, *27*, No. 1703779.
- (42) Li, X.; Kou, Z.; Xi, S.; Zang, W.; Yang, T.; Zhang, L.; Wang, J. Porous NiCo<sub>2</sub>S<sub>4</sub>/FeOOH Nanowire Arrays with Rich Sulfide/Hydroxide Interfaces Enable High OER Activity. *Nano Energy* **2020**, *78*, No. 105230.
- (43) Fei, H.; Guo, T.; Xin, Y.; Wang, L.; Liu, R.; Wang, D.; Liu, F.; Wu, Z. Sulfur Vacancy Engineering of MoS<sub>2</sub> via Phosphorus Incorporation for Improved Electrocatalytic N<sub>2</sub> Reduction to NH<sub>3</sub>. *Appl. Catal. B Environ.* **2022**, *300*, No. 120733.
- (44) Tao, Y.; Yuan, J.; Qian, X.; Meng, Q.; Zhu, J.; He, G.; Chen, H. Spinel-Type FeNi<sub>2</sub>S<sub>4</sub> with Rich Sulfur Vacancies Grown on Reduced Graphene Oxide toward Enhanced Supercapacitive Performance. *Inorg. Chem. Front.* **2021**, *8*, 2271.
- (45) Wu, F.; Yang, R.; Lu, S.; Du, W.; Zhang, B.; Shi, Y. Unveiling Partial Transformation and Activity Origin of Sulfur Vacancies for Hydrogen Evolution. *ACS Energy Lett.* **2022**, *7*, 4198.
- (46) Peng, Q.; He, Q.; Hu, Y.; Isimjan, T. T.; Hou, R.; Yang, X. Interface Engineering of Porous Fe<sub>2</sub>P–WO<sub>2.92</sub> Catalyst with Oxygen Vacancies for Highly Active and Stable Large-Current Oxygen Evolution and Overall Water Splitting. *J. Energy Chem.* **2022**, *65*, 574.
- (47) Hu, Y.; Luo, Z.; Guo, M.; Dong, J.; Yan, P.; Hu, C.; Isimjan, T. T.; Yang, X. Interface Engineering of Co<sub>2</sub>N<sub>0.67</sub>/CoMoO<sub>4</sub> Heterostructure Nanosheets as a Highly Active Electrocatalyst for Overall Water Splitting and Zn–H<sub>2</sub>O Cell. *Chem. Eng. J.* **2022**, *435*, No. 134795.
- (48) Peng, Q.; Shao, X.; Hu, C.; Luo, Z.; Taylor Isimjan, T.; Dou, Z.; Hou, R.; Yang, X. Co<sub>4</sub>S<sub>3</sub> Grafted 1 T-Phase Dominated WS<sub>2</sub> Ultrathin Nanosheet Arrays for Highly Efficient Overall Water Splitting in Alkaline Media. *J. Colloid Interface Sci.* **2022**, *615*, 577.
- (49) Hu, Y.; Zheng, Y.; Jin, J.; Wang, Y.; Peng, Y.; Yin, J.; Shen, W.; Hou, Y.; Zhu, L.; An, L.; et al. Understanding the Sulphur–Oxygen Exchange Process of Metal Sulphides Prior to Oxygen Evolution Reaction. *Nat. Commun.* **2023**, *14*, 1949.
- (50) Chen, R.; Zhang, Z.; Wang, Z.; Wu, W.; Du, S.; Zhu, W.; Lv, H.; Cheng, N. Constructing Air-Stable and Reconstruction-Inhibited Transition Metal Sulfide Catalysts via Tailoring Electron-Deficient Distribution for Water Oxidation. *ACS Catal.* **2022**, *12*, 13234.
- (51) Friebe, D.; Louie, M. W.; Bajdich, M.; Sanwald, K. E.; Cai, Y.; Wise, A. M.; Cheng, M.-J.; Sokaras, D.; Weng, T.-C.; Alonso-Mori, R.; et al. Identification of Highly Active Fe Sites in (Ni,Fe)OOH for Electrocatalytic Water Splitting. *J. Am. Chem. Soc.* **2015**, *137*, 1305.
- (52) Wang, Y.; Li, X.; Zhang, M.; Zhang, J.; Chen, Z.; Zheng, X.; Tian, Z.; Zhao, N.; Han, X.; Zaghbi, K.; et al. Highly Active and Durable Single-Atom Tungsten-Doped NiS<sub>0.5</sub>Se<sub>0.5</sub> Nanosheet @ NiS<sub>0.5</sub>Se<sub>0.5</sub> Nanorod Heterostructures for Water Splitting. *Adv. Mater.* **2022**, *34*, No. 2107053.
- (53) Chen, Z.; Zheng, R.; Deng, S.; Wei, W.; Wei, W.; Ni, B.-J.; Chen, H. Modular Design of an Efficient Heterostructured FeS<sub>2</sub>/TiO<sub>2</sub> Oxygen Evolution Electrocatalyst via Sulfidation of Natural Ilmenites. *J. Mater. Chem. A* **2021**, *9*, 25032.
- (54) Wu, L.; Ning, M.; Xing, X.; Wang, Y.; Zhang, F.; Gao, G.; Song, S.; Wang, D.; Yuan, C.; Yu, L.; et al. Boosting Oxygen Evolution Reaction of (Fe,Ni)OOH via Defect Engineering for Anion Exchange Membrane Water Electrolysis Under Industrial Conditions. *Adv. Mater.* **2023**, *35*, No. 2306097.
- (55) Sun, S.-C.; Ma, F.-X.; Li, Y.; Dong, L.-W.; Liu, H.; Jiang, C.-M.; Song, B.; Zhen, L.; Xu, C.-Y. Sulfur Vacancies Promoting Fe-Doped Ni<sub>3</sub>S<sub>2</sub> Nanopyramid Arrays as Efficient Bifunctional Electrocatalysts for Overall Water Splitting. *Sustain. Energy Fuels* **2020**, *4*, 3326–3333.